

imental evidence. From this measurement, we also learn that the electric field points toward the electron detector at the pulse peak and that its strength is  $\sim 7 \times 10^7$  V/cm. With the temporal evolution, strength, and direction of  $E_{\perp}(t)$  measured, we have performed a complete characterization of a light pulse in terms of its classical electric field.

Direct probing of light-field oscillations represents what we believe to be a substantial extension of the basic repertoire of modern experimental science. The door to practical applications is opened by the creation of the key element of the demonstrated light-field detector, the synchronized attosecond electron probe, in a noninvasive manner. In fact, our intense  $<5$ -fs laser pulse appears to be capable of producing the necessary XUV trigger burst without suffering any noticeable back-action to its own temporal shape (Fig. 3). After having produced the attosecond photon probe, this powerful few-femtosecond pulse is ideally suited for the synthesis of ultrabroadband, few-cycle, optical waveforms (5–17). Being composed of radiation extending from the infrared through the visible to the ultraviolet region, the resultant few-cycle, monocycle, and conceivably even subcycle waveforms will offer a marked degree of control over the temporal variation of electric and magnetic forces on molecular and atomic time scales.

These light forces, in turn, afford the promise of controlling quantum transitions of electrons in atoms and molecules and—at relativistic intensities—their center-of-mass motion. Reproducible ultrabroadband light wave synthesis, a prerequisite for these prospects to materialize, is inconceivable without subfemtosecond measurement of the synthesized waveforms. Beyond providing the subfemtosecond electron probe for these measurements, the substantial experimental efforts associated with the construction and reliable operation of a subfemtosecond photon source will pay off in yet another way. The envisioned control of electronic motion with light forces can only be regarded as accomplished once it has been measured. Owing to their perfect synchronism with the synthesized light waveforms, the subfemtosecond photon probe will allow us to test the degree of control achieved by tracking the triggered (and hopefully steered) motion in a time-resolved fashion.

#### References and Notes

1. R. Trebino *et al.*, *Rev. Sci. Instrum.* **68**, 3277 (1997).
2. C. Iaconis, I. A. Walmsley, *Opt. Lett.* **23**, 792 (1998).
3. G. G. Paulus *et al.*, *Phys. Rev. Lett.* **91**, 253004 (2003).
4. T. Brabec, F. Krausz, *Phys. Rev. Lett.* **78**, 3282 (1997).
5. T. W. Hänsch, *Opt. Commun.* **80**, 71 (1990).
6. S. Yoshikawa, T. Imasaka, *Opt. Commun.* **96**, 94 (1993).
7. A. E. Kaplan, P. L. Shkolnikov, *Phys. Rev. Lett.* **73**, 1243 (1994).
8. K. Shimoda, *Jpn. J. Appl. Phys.* **34**, 3566 (1995).
9. S. E. Harris, A. V. Sokolov, *Phys. Rev. Lett.* **81**, 2894 (1998).
10. A. Nazarkin, G. Korn, *Phys. Rev. Lett.* **83**, 4748 (1999).
11. O. Albert, G. Mourou, *Appl. Phys. B* **69**, 207 (1999).

12. M. Wittman, A. Nazarkin, G. Korn, *Phys. Rev. Lett.* **84**, 5508 (2000).
13. Y. Kobayashi, K. Torizuka, *Opt. Lett.* **25**, 856 (2000).
14. A. V. Sokolov, D. R. Walker, D. D. Yavuz, G. Y. Yin, S. E. Harris, *Phys. Rev. Lett.* **87**, 033402 (2001).
15. K. Yamane *et al.*, *Opt. Lett.* **28**, 2258 (2003).
16. M. Y. Shverdin, D. R. Walker, D. D. Yavuz, G. Y. Yin, S. E. Harris, in *OSA Trends in Optics and Photonics Series (TOPS) Vol. 96, Conference on Lasers and Electro-Optics (CLEO)* (Optical Society of America, Washington, DC, 2004), Postdeadline paper CPDC1.
17. K. Yamane, T. Kito, R. Morita, M. Yamashita, in *OSA Trends in Optics and Photonics Series (TOPS)*, vol. 96, *Conference on Lasers and Electro-Optics (CLEO)*, (Optical Society of America, Washington, DC, 2004), Postdeadline paper CPDC2.
18. R. Kienberger *et al.*, *Science* **297**, 1144 (2002).
19. A. D. Bandrauk, Sz. Chelkowski, N. H. Shon, *Phys. Rev. Lett.* **89**, 283903 (2002).
20. A. Baltuska *et al.*, *Nature* **421**, 611 (2003).
21. R. Kienberger *et al.*, *Nature* **427**, 817 (2004).
22. In the limit of  $|\Delta p_{\max}| \ll |p_i|$ , the change in the electrons' final kinetic energy is given by  $\Delta W_{\max} \approx [8W/U_{p,\max}]^{1/2}$ , where  $U_{p,\max} = e^2 E_0^2 / 4m_e \omega_L^2$  is the electrons' quiver energy averaged over an optical cycle at the peak of the light pulse.
23. Increase of the excitation energy  $\hbar\omega_{\text{XUV}}$  tends to reconcile the conflicting requirements of avoiding field ionization and ensuring a high dynamic range.
24. T. Brabec, F. Krausz, *Rev. Mod. Phys.* **72**, 545 (2000).
25. We are grateful to B. Ferus for creating the artwork. Sponsored by the fonds zur Förderung der Wissenschaftlichen Forschung (Austria, grant nos. Y44-PHY, P15382, and F016), the Deutsche Forschungsgemeinschaft and the Volkswagenstiftung (Germany), the European ATTO and Ultrashort XUV Pulses for Time-Resolved and Non-Linear Applications networks, and an Austrian Programme for Advanced Research and Technology fellowship to R.K. from the Austrian Academy of Sciences.

28 May 2004; accepted 20 July 2004

## Nanoribbon Waveguides for Subwavelength Photonics Integration

Matt Law,<sup>1,2\*</sup> Donald J. Sirbuly,<sup>1,2\*</sup> Justin C. Johnson,<sup>1</sup> Josh Goldberger,<sup>1</sup> Richard J. Saykally,<sup>1</sup> Peidong Yang<sup>1,2†</sup>

Although the electrical integration of chemically synthesized waveguides has been achieved with lithography, optical integration, which promises high speeds and greater device versatility, remains unexplored. We describe the properties and functions of individual crystalline oxide nanoribbons that act as subwavelength optical waveguides and assess their applicability as nanoscale photonic elements. The length, flexibility, and strength of these structures enable their manipulation on surfaces, including the optical linking of nanoribbon waveguides and other nanowire elements to form networks and device components. We demonstrate the assembly of ribbon waveguides with nanowire light sources and detectors as a first step toward building nanowire photonic circuitry.

Photonics, the optical analog of electronics, shares the logic of miniaturization that drives research in semiconductor and information technology. The ability to manipulate pulses of light within sub-micrometer volumes is vital for highly integrated light-based devices, such as optical computers, to be realized. Recent advances in the use of photonic band gap (1, 2) and plasmonic (3, 4) phenomena to control the flow of light are impressive in this regard. One alternative route to integrated photonics is to assemble photonic circuits from a collection of nanowire elements that assume different functions, such as light creation, routing, and detection. Chemically synthesized nanowires have several features that make them good photonic building blocks, including inherent one-dimensionality, a di-

versity of optical and electrical properties, good size control, low surface roughness, and, in principle, the ability to operate above and below the diffraction limit. The toolbox of nanowire device elements already includes various types of transistors (5), light-emitting diodes (6), lasers (7, 8), and photodetectors (9). An important step toward nanowire photonics is to develop a nanowire waveguide that can link these various elements and provide the flexibility in interconnection patterns that is needed to carry out complex tasks such as logic operations (10). Our demonstration of nanowire-based photonics complements and expands upon recent work on optical beam steering in mesostructured silica cavities (11) and on subwavelength structures made lithographically (12, 13) and by the drawing of silica microfibers (14).

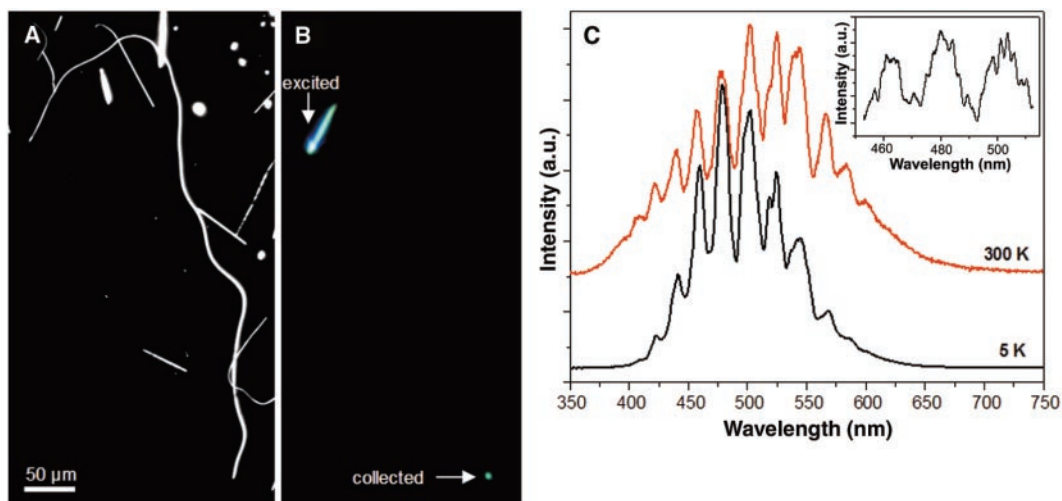
Nanoscale ribbon-shaped crystals of binary oxides exhibit a range of interesting properties including extreme mechanical flexibility, surface-mediated electrical conductivity (15), and lasing (16). As part of a recent study of the photoluminescence (PL) of SnO<sub>2</sub> nanoribbons, we noted that ribbons with high

<sup>1</sup>Department of Chemistry, University of California, Berkeley, CA 94720, USA. <sup>2</sup>Materials Science Division, Lawrence Berkeley National Laboratory, 1 Cyclotron Road, Berkeley, CA 94720, USA.

\*These authors contributed equally to this work.

†To whom correspondence should be addressed. E-mail: p\_yang@uclink.berkeley.edu

**Fig. 1.** Optical waveguiding in a 715- $\mu\text{m}$ -long  $\text{SnO}_2$  nanoribbon. (A) A dark-field image of the meandering ribbon (350 nm wide by 245 nm thick) and its surroundings. (B) The PL image of the waveguiding nanoribbon under laser excitation. The laser is focused to a spot size of  $\sim 50 \mu\text{m}$  ( $30^\circ$  incidence angle) at the top end of the ribbon. (C) Spectra of the emission from the bottom terminus of the waveguide, collected at room temperature and 5 K. The mode structure does not change substantially with temperature, suggesting minimal dependence on index of refraction variations. A higher resolution emission profile (inset) shows fine structure in three of the central peaks. This fine structure is present in every peak. a.u., arbitrary units.

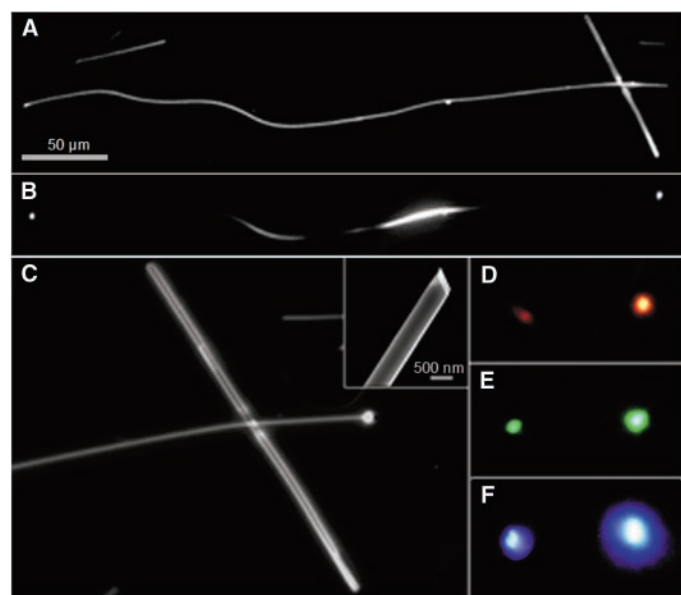


aspect ratios ( $>1000$ ) act as excellent waveguides of their visible PL emission.  $\text{SnO}_2$  is a wide band gap (3.6 eV) semiconductor characterized by defect-related PL bands at 2.5 eV (green) and 2.1 eV (orange) and finds application in gas sensors and transparent electrodes. We used a thermal transport process (17) to synthesize single-crystalline nanoribbons of  $\text{SnO}_2$  with lengths of up to 1500  $\mu\text{m}$ . These structures possess fairly uniform ( $\pm 10\%$ ) rectangular cross sections with dimensions as large as 2  $\mu\text{m}$  by 1  $\mu\text{m}$  and as small as 15 nm by 5 nm. Many of the ribbons are 100 to 400 nm wide and thick, an optimal size range for efficient steering of visible and ultraviolet (UV) light within a subwavelength cavity.

The waveguiding behavior of individual nanoribbons dispersed on  $\text{SiO}_2$  and mica substrates was studied with the use of far-field microscopy and spectroscopy (18). Figures 1 and 2 show representative data collected from single ribbons with lengths of 715 and 425  $\mu\text{m}$ , respectively. When we focused continuous wave laser light (3.8 eV) onto one end of a ribbon, the generated PL was strongly guided by the cavity to emanate with high intensity at its opposite end, mimicking a conventional optical fiber. Ribbons that possessed sizeable surface defects (i.e., large step edges or attached particulates) scattered guided light in a series of bright spots along their lengths. Contact points between ribbons were often dark, although overlying ribbons sometimes acted as scattering centers (Fig. 2C).

Typically, an emission spectrum collected from the end of a ribbon features complex, quasi-periodic modulation (Fig. 1C) that results from the interference of electromagnetic waves resonating within the rectangular cavity (i.e., an optical mode structure). In short nanowire waveguides,

**Fig. 2.** Panchromatic waveguiding in a 425- $\mu\text{m}$ -long ribbon. (A) Dark-field image. Cross-sectional dimensions are 520 nm by 275 nm. (B) PL image with the UV excitation spot centered near the middle of the ribbon, showing waveguided emission from both ends. (C) Magnified dark-field PL view of the right end, with the laser focused on the left end. A wide ( $\sim 1 \mu\text{m}$ ) ribbon lies across the ribbon of interest. (Inset) A scanning electron micrograph of the right terminus of the nanoribbon, showing its rectangular cross section. (D to F) Digital images of the guided emission during nonresonant excitation with monochromatic red, green, and blue light, respectively. The leftmost emission spot, caused by scattering at the ribbon-ribbon junction, can be eliminated by selectively removing the wide ribbon with the micromanipulator.



such modulation is attributed to longitudinal Fabry-Perot-type modes, with a mode spacing,  $\Delta\lambda$ , given by  $\Delta\lambda = \lambda^2 / \{2L[n - \lambda(dn/d\lambda)]\}$ , where  $\lambda$  is the wavelength,  $L$  is the cavity length, and  $n$  is the index of refraction (2.1 for  $\text{SnO}_2$ ). The nanoribbons, however, are so long that  $\Delta\lambda$  is below the resolution limit of our instrument (0.1 nm). In addition,  $\text{SnO}_2$  cavities are unlikely to show longitudinal modes, because the reflectivity of their end facets is low ( $\leq 13\%$ ) and there is no gain to compensate for scattering and output-coupling losses. We have yet to identify the observed modulation with specific transverse or bow-tie (19) modes. A systematic study of the spectral structure is complicated by the intricate dependence of the modes on ribbon cross-

sectional size and orientation (through bend losses, substrate coupling, and variations in refractive index) as well as on light intensity and end facet roughness. We note that the existence of a mode structure indicates that nanoribbon cavities can have high finesse and show that the transmission at given wavelengths can be modified by distorting the cavity shape. Numerical simulations are now being applied to better understand the origin of this wavelength modulation.

In general, one would expect a subwavelength waveguide to show a large optical loss that is highly wavelength-dependent, with better confinement of shorter wavelength radiation. We illuminated single nanoribbons with monochromatic red, green, and blue light and established that red

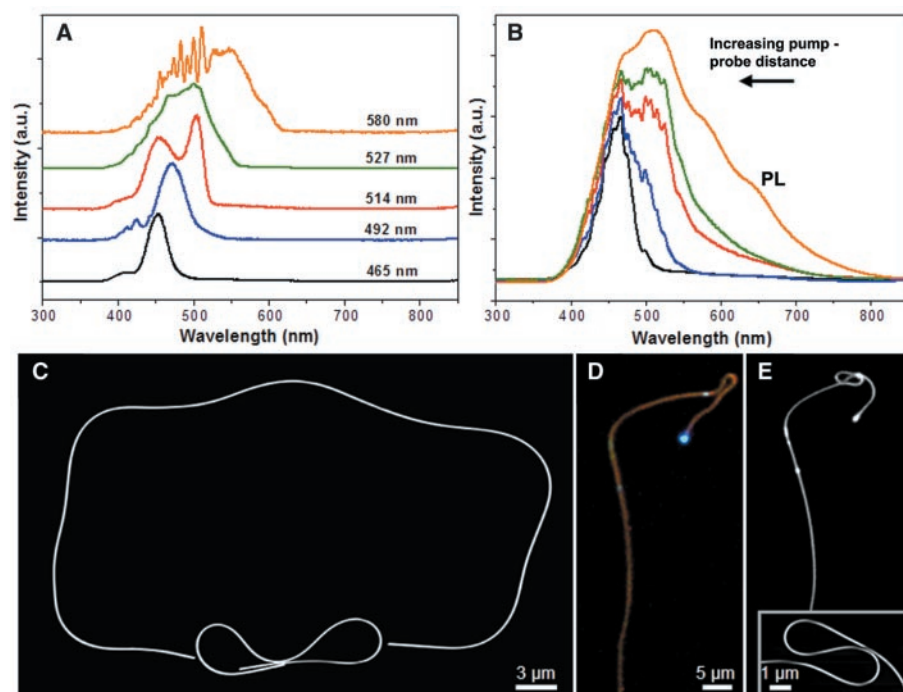


**Fig. 3.** Nanoribbon short-pass filters and shape manipulation. (A) Room-temperature PL spectra of five different nanoribbons, each 200 to 400  $\mu\text{m}$  long, with 50% intensity cutoff wavelengths ranging from 465 to 580 nm. Cross-sectional dimensions of the 465, 492, 514, 527, and 580 nm filters are 310 nm by 100 nm ( $0.031 \mu\text{m}^2$ ), 280 nm by 120 nm ( $0.034 \mu\text{m}^2$ ), 350 nm by 115 nm ( $0.040 \mu\text{m}^2$ ), 250 nm by 225 nm ( $0.056 \mu\text{m}^2$ ), and 375 by 140 nm ( $0.052 \mu\text{m}^2$ ), respectively. Spectra are normalized and offset for clarity. (B) A series of normalized emission spectra taken of a single nanoribbon (315  $\mu\text{m}$  by 355 nm by 110 nm) as the pump spot was scanned away from the collection area. The unguided PL curve was obtained at a pump-probe separation of 50  $\mu\text{m}$ . Larger separations result in a progressive loss of the long wavelengths. (C) An SEM image of a simple shape, demonstrating the high level of positional control afforded by the micromanipulator. This shape was created from a single straight ribbon (dimensions of 400 nm by 115 nm) that was cut into two pieces and then assembled. (D and E) Optical images of the emission end of a long nanoribbon (aspect ratio = 5200), showing the minimal effect of curvature on waveguiding. (D) A true-color photograph taken after crafting a single bend. (E) A black-and-white dark-field PL image captured after an S turn was completed. Blue light is guided around both 1  $\mu\text{m}$  radii curves. An SEM image (inset) resolves the bent geometry. The scattering center on the bend is because of a step edge rather than physical contact.

waveguiding was rare; green, common; and blue, ubiquitous. For a given dielectric material and cavity geometry and wavelength, there exists a critical diameter below which all higher order optical modes are cut off and waveguiding becomes increasingly difficult to sustain. If a nanoribbon is treated as a cylinder of  $\text{SnO}_2$  embedded in air, we find cutoff diameters for higher order transverse modes of about 270, 220, and 180 nm for the 652-, 532-, and 442-nm light used in our experiment (20). Although this approximation simplifies the cavity shape and ignores substrate coupling and other effects, these values are in reasonable agreement with scanning electron microscope (SEM) measurements of the blue and green waveguide sizes. Most of the ribbons in our samples are too thin to propagate red light over distances greater than 100  $\mu\text{m}$ . However, sufficiently large ribbons guide wavelengths across the visible spectrum, acting as subwavelength red-green-blue optical fibers (Fig. 2, D to F).

The approximate size of a nanoribbon can be inferred from the color of its guided PL; large ribbons are white, whereas small ribbons are blue. When a ribbon of average size is pumped nearer to one end, it shines blue at the far end and green at the near end, demonstrating the higher radiation losses for longer wavelengths. This effect makes nanoribbons excellent short-pass filters with tunable cutoffs based on path length. We have identified ribbon filters spanning the 465- to 580-nm region that feature steep cutoff edges and virtually zero transmission of blocked wavelengths (Fig. 3, A and B).

We quantified the wavelength-dependent loss of long, straight ribbons with the use of near-field scanning optical microscopy (NSOM). Ribbons were pumped with a tightly focused laser beam (3.8 eV) at different points along their lengths relative to a NSOM collection tip held stationary over one of their ends. Directly exciting the semiconductor waveguide in this way cre-

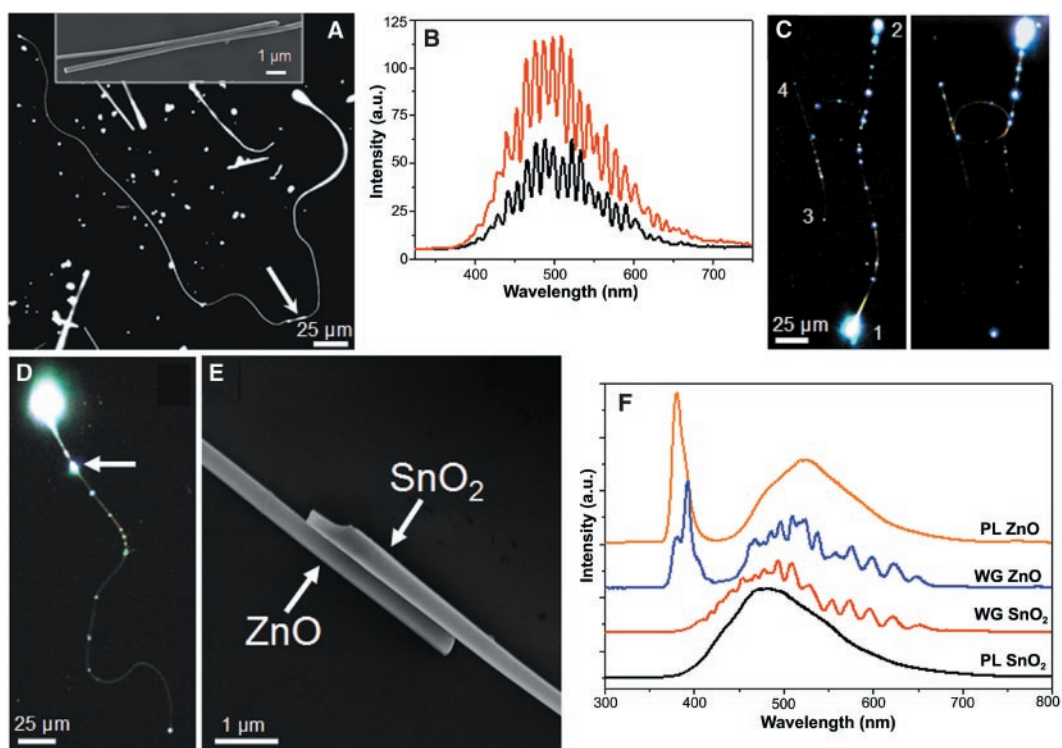
ated a consistent amount of light in the cavity for each measurement, avoiding the difficulty of inserting light from a second fiber with a constant insertion efficiency. Losses ranged from 1 to 8  $\text{dB mm}^{-1}$  for wavelengths between 450 and 550 nm, depending on ribbon cross-sectional area and the density of scattering centers. These values are higher than those reported recently for subwavelength silica waveguides (14), mainly because of substrate-induced radiation loss and, in some cases, the existence of minor scattering crystal steps and terraces along the nanoribbon surface. We note, however, that the losses here are much better than what is required for integrated planar photonic applications, in which waveguide elements would transmit light over sub-micrometer distances.

The nanoribbons are of sufficient length and strength to be pushed, bent, and shaped with the use of a commercial micromanipulator under an optical microscope. Free-standing ribbons can be repeatedly and elastically curved into loops with radii as small as 5  $\mu\text{m}$ , which is remarkable for a crystal that is brittle in its bulk form (21). On appropriately chosen surfaces, single ribbons are easily fashioned into a variety of shapes with the help of ribbon-substrate forces to prevent elastic recoil (Fig. 3C). Careful manipulation is normally nondestructive to the ribbon cavities. In practice, this manipulation method is applicable to nanostructures that are free to move and visible with dark-field microscopy, including, at the lower size limit, short nanowires (40 nm by 3  $\mu\text{m}$ ) and even large nanocrystals. Although an inherently slow serial process, it is faster and more versatile than similar approaches using, for instance, scanning probes (22) or in situ SEM manipulation (23). We can create networks of nanoribbon waveguides and build functioning optoelectronic components by assembling individual nanowire elements one at a time.

Manipulation also makes it possible to investigate the shape-dependent waveguiding of single nanoribbon cavities. For example, we fashioned a tight S turn in one end of a long, thin ribbon (dimensions of 785  $\mu\text{m}$  by 275 nm by 150 nm) to illustrate the robust nature of optical steering in these structures (Fig. 3, D and E). Although losses around the bends could not be measured in this case, they were small enough to only minimally reduce light output from the end of the ribbon. In general, twists and bends with radii of curvature as small as 1  $\mu\text{m}$  do not disrupt the ability of these subwavelength waveguides to channel light across hundreds of micrometers.

Bending a nanoribbon, even slightly, can dramatically change the mode structure of its output light (fig. S1). This is most likely

**Fig. 4.** Nanoribbon coupling and optical components. (A) A black-and-white dark-field PL image of two coupled ribbons (both ribbons are 750 nm by 250 nm, 630  $\mu\text{m}$  total length). Light is incident on the right terminus of the right ribbon and collected at the left terminus of the left ribbon. The arrow denotes the location of the junction. An SEM image (inset) resolves the junction layout. (B) Raw emission spectra of the left ribbon before (red) and after (black) forming the junction. The addition of the second ribbon and the junction lowers the output light intensity by only 50%, whereas its modulation is retained. (C) True-color dark-field PL images of a three-ribbon ring structure that functions as a directional coupler. The ring ribbon (135  $\mu\text{m}$  by 540 nm by 175 nm) is flanked by two linear ribbons (left, 120  $\mu\text{m}$  by 540 nm by 250 nm; right, 275  $\mu\text{m}$  by 420 nm by 235 nm). Light input at branch 1 exits preferentially at branch 3 (left), whereas light input at branch 2 exits branch 4 (right). See fig. S2 for a dark-field image of the structure. (D) A true-color dark-field PL image of a ZnO nanowire (56  $\mu\text{m}$  long, at top, pumped at 3.8 eV) channeling light into a SnO<sub>2</sub> nanoribbon (265  $\mu\text{m}$  long, at bottom). The arrow denotes the location of the junction. (E) An SEM image of the wire-ribbon junction. (F) Spectra of the coupled structures taken at different excitation and collection locations. From top to



bottom: unguided PL of the nanowire, waveguided (WG) emission from the ZnO wire collected at the bottom terminus of the ribbon, waveguided emission from the SnO<sub>2</sub> ribbon excited just below the junction and collected at its bottom terminus, and unguided PL of the ribbon. The emission from the ZnO nanowire is modulated during its transit through the nanoribbon cavity.

bottom: unguided PL of the nanowire, waveguided (WG) emission from the ZnO wire collected at the bottom terminus of the ribbon, waveguided emission from the SnO<sub>2</sub> ribbon excited just below the junction and collected at its bottom terminus, and unguided PL of the ribbon. The emission from the ZnO nanowire is modulated during its transit through the nanoribbon cavity.

because a change in cavity curvature and/or cavity-substrate coupling alters the interference pattern of propagating waves, resulting in the enhancement of some modes and the partial quenching of others. Our data also indicate that the emission pattern from a typical nanoribbon is spatially heterogeneous, as shown previously in ZnO nanowires (24). As a consequence, the far-field spectrum changes somewhat with collection angle, though not enough to account for the complex modal variations seen in response to distortions of the cavity shape.

Nanoribbon waveguides can be coupled together to create optical networks that may form the basis of miniaturized photonic circuitry. Because light diffracts in all directions when it emerges from a subwavelength aperture, nanoribbons must be in close proximity, and preferably in direct physical contact, to enable the efficient transfer of light between them. We tested various coupling geometries and found that a staggered side-by-side arrangement, in which two ribbons interact over a distance of several micrometers, outperforms direct end-to-end coupling, which relies on scattering between end facets. Staggered ribbons separated by a thin air gap can communicate via tunneling of evanescent waves (25). It is also possible to bond two

ribbons together by van der Waals forces, often simply by draping one over another, to create a robust optical junction. Figure 4, A and B, shows an example of two-ribbon coupling. More functional geometries (26), such as Y junctions, branch networks, Mach-Zehnder interferometers, and ring oscillators can also be constructed. The three-ribbon ring structure in Fig. 4C operates by circulating light that is injected from one branch around a central cavity, which can be tapped by one or more output channels to act as an optical hub. With further integration, it should be possible to create optical modulators based on nanoribbon assemblies that use the electrooptic effect for phase shifting (27).

Nanowire light sources and optical detectors can be linked to ribbon waveguides to create input and output components for future photonic devices. Figure 4D shows light injection into a ribbon cavity by an optically pumped ZnO nanowire. The ribbon imprints its mode profile on both the UV and visible emission of the nanowire (Fig. 4F), demonstrating the propagation and modulation of a quasi-Gaussian light beam in a subwavelength optical cavity. In the opposite configuration, PL from a nanoribbon can be detected electrically by a ZnO nanowire positioned at its end (fig. S3). It is possible for ZnO to act

as a detector in this case because it can weakly absorb sub-band gap light (28). We used a NSOM tip to excite the nanoribbon locally and thereby provide sufficient spatial resolution to detect waveguided light amid the background laser light scattered onto the wire detector. Scanning the NSOM tip on and off the ribbon caused photocurrent oscillations within the detector. Moreover, the oscillations ceased when the end of the ribbon was moved away from the nanowire detector. These results demonstrate the feasibility of nanowire-based photonic circuitry. Practical devices will require the integration of ribbon waveguides with electrically driven nanowire light sources and a variety of high-performance detector elements with different band gaps.

Single-crystalline nanoribbons are intriguing structures with which to manipulate light, both for fundamental studies and photonics applications. As passive elements, they are efficient UV and visible waveguides and filters that can be assembled into optical networks and components. Being semiconductors or, in their doped state, transparent metals, oxide nanoribbons are well suited to combine simultaneous electron and photon transport in active nanoscale components. Key challenges to the wider use of these materials include narrowing their size dispersity and devel-

oping better parallel assembly schemes for nanowire integration (29).

### References and Notes

- S. Noda, K. Tomoda, N. Yamamoto, A. Chutinan, *Science* **289**, 604 (2000).
- C. López, *Adv. Mater.* **15**, 1679 (2003).
- W. L. Barnes, A. Dereux, T. W. Ebbesen, *Nature* **424**, 824 (2003).
- J. R. Krenn, J.-C. Weeber, *Philos. Trans. R. Soc. Lond. A* **362**, 739 (2004).
- X. Duan *et al.*, *Nature* **425**, 274 (2003).
- M. C. McAlpine *et al.*, *Nano Lett.* **3**, 1531 (2003).
- M. H. Huang *et al.*, *Science* **292**, 1897 (2001).
- X. Duan, Y. Huang, R. Agarwal, C. M. Lieber, *Nature* **421**, 241 (2003).
- H. Kind, H. Yan, B. Messer, M. Law, P. Yang, *Adv. Mater.* **14**, 158 (2002).
- D. Psaltis, *Science* **298**, 1359 (2002).
- P. Yang *et al.*, *Science* **287**, 465 (2000).
- R. Quidant *et al.*, *Phys. Rev. E* **64**, 066607 (2001).
- V. R. Almeida, Q. Xu, C. A. Barrios, M. Lipson, *Opt. Lett.* **29**, 1209 (2004).
- L. Tong *et al.*, *Nature* **426**, 816 (2003).
- M. Law, H. Kind, B. Messer, F. Kim, P. Yang, *Angew. Chem. Int. Ed. Engl.* **41**, 2405 (2002).
- H. Yan *et al.*, *Adv. Mater.* **15**, 1907 (2003).
- Z. W. Pan, Z. R. Dai, Z. L. Wang, *Science* **291**, 1947 (2001).
- Materials and methods are available as supporting material on *Science* Online.
- C. Gmachl *et al.*, *Science* **280**, 1556 (1998).
- A. W. Snyder, D. Love, *Optical Waveguide Theory* (Kluwer, Boston, 1983).
- We also have observed extremely convoluted "wet noodle" shapes in the case of thin (<50 nm) non-waveguiding nanoribbons dispersed on surfaces, including loops with radii of 100 nm.
- H. W. C. Postma, A. Sellmeijer, C. Dekker, *Adv. Mater.* **12**, 1299 (2000).
- K. Kim *et al.*, *Rev. Sci. Instrum.* **74**, 4021 (2003).
- J. C. Johnson, H. Yan, P. Yang, R. J. Saykally, *J. Phys. Chem. B* **107**, 8816 (2003).
- R. C. Reddick, R. J. Warmack, D. W. Chilcott, S. L. Sharp, T. L. Ferrell, *Rev. Sci. Instrum.* **61**, 3669 (1990).
- K. Okamoto, *Fundamentals of Optical Waveguides* (Academic Press, San Diego, CA, 2000).
- L. Eldada, *Rev. Sci. Instrum.* **75**, 575 (2004).
- H. J. Egelhaaf, D. Oelkrug, *J. Cryst. Growth* **161**, 190 (1996).
- A. Tao *et al.*, *Nano Lett.* **3**, 1229 (2003).
- This work was supported in part by the Camille and Henry Dreyfus Foundation, the Alfred P. Sloan Foundation, the Beckman Foundation, the U.S. Department of Energy, and NSF. J.G. thanks NSF for a graduate research fellowship. Work at the Lawrence Berkeley National Laboratory was supported by the Office of Science, Basic Energy Sciences, Division of Materials Science of the U. S. Department of Energy. We thank H. Yan for the ZnO nanowires and the National Center for Electron Microscopy for the use of their facilities.

### Supporting Online Material

www.sciencemag.org/cgi/content/full/305/5688/1269/DC1

Materials and Methods  
Figs. S1 to S3

2 June 2004; accepted 15 July 2004

# Transparent, Conductive Carbon Nanotube Films

Zhuangchun Wu,<sup>1\*</sup> Zhihong Chen,<sup>1\*†</sup> Xu Du,<sup>1</sup>  
Jonathan M. Logan,<sup>1</sup> Jennifer Sippel,<sup>1</sup> Maria Nikolou,<sup>1</sup>  
Katalin Kamaras,<sup>2</sup> John R. Reynolds,<sup>3</sup> David B. Tanner,<sup>1</sup>  
Arthur F. Hebard,<sup>1</sup> Andrew G. Rinzler<sup>1‡</sup>

We describe a simple process for the fabrication of ultrathin, transparent, optically homogeneous, electrically conducting films of pure single-walled carbon nanotubes and the transfer of those films to various substrates. For equivalent sheet resistance, the films exhibit optical transmittance comparable to that of commercial indium tin oxide in the visible spectrum, but far superior transmittance in the technologically relevant 2- to 5-micrometer infrared spectral band. These characteristics indicate broad applicability of the films for electrical coupling in photonic devices. In an example application, the films are used to construct an electric field-activated optical modulator, which constitutes an optical analog to the nanotube-based field effect transistor.

Transparent electrical conductors pervade modern technologies, providing a critical component of video displays, video and still-image recorders, solar cells, lasers, optical communication devices, and solid-state lighting [for recent reviews, see (1, 2)]. We describe a class of transparent conducting material based on continuous films of pure single-walled carbon nanotubes (SWNTs). These intrinsic electrical conductors are formed into uniform, optically homogeneous films of controllable thickness that are thin enough to be transparent over technologically relevant regions of the

electromagnetic spectrum. Use of the transparent SWNT films (t-SWNTs) for current injection into p-GaN and for blue light-emitting GaN/InGaN diodes (light extracted through the films) has recently been demonstrated, together with patterning of the t-SWNTs by standard microlithographic techniques (3). Here we elaborate on the film production process, transfer to substrates, film morphology, and electrical and optical properties. We also demonstrate use of the t-SWNTs as the active element of an optical modulator. This constitutes an optical analog to the SWNT-based field-effect transistor (FET), modulating light transmission through the films by application of electric fields.

Other methods of transparent nanotube film production include drop-drying from solvent, airbrushing, and Langmuir-Blodgett deposition. These alternatives, however, present severe limitations in terms of the film quality or production

efficiency (4). Our t-SWNT production process is quite simple, comprising three steps: (i) vacuum-filtering a dilute, surfactant-based suspension of purified nanotubes onto a filtration membrane (forming the homogeneous film on the membrane); (ii) washing away the surfactant with purified water; and (iii) dissolving the filtration membrane in solvent (4). Multiple techniques for transfer of the film to the desired substrate have been developed. The films can be made free-standing over appreciable apertures (~1 cm<sup>2</sup>) by making the transfer to a substrate with a hole, over which the film is laid before membrane dissolution (5, 6).

This filtration method has several advantages: (i) Homogeneity of the films is guaranteed by the process itself. As the nanotubes accumulate, they generate a filter cake that acts to impede the permeation rate. If a region becomes thicker, the local permeation rate and associated deposition rate slow down, allowing thinner regions to catch up. (ii) Because of their extreme rigidity (for objects of such small diameters), the nanotubes have long persistence lengths. They consequently tend to lie straight, gaining maximal overlap and interpenetration within the film as they accumulate (the curvature observed in Fig. 1D is likely caused by van der Waals forces dominating as the surfactant is washed away). This yields maximal electrical conductivity and mechanical integrity throughout the films. (iii) The film thickness is readily controlled, with nanoscale precision, by the nanotube concentration and volume of the suspension filtered.

Examples of the transparent films are shown in Fig. 1. Films of thickness 50 and 150 nm, as measured by atomic force microscopy (AFM) at step edges, display a corresponding increase in optical density (Fig. 1A). Films as large as 10 cm in diam-

Departments of <sup>1</sup>Physics and <sup>3</sup>Chemistry, University of Florida, Gainesville, FL 32611, USA. <sup>2</sup>MTA SzFKI, Budapest, H 1525, Hungary.

\*These authors contributed equally to this work.

†Present address: IBM T. J. Watson Research Center, Yorktown Heights, NY 10598, USA.

‡To whom correspondence should be addressed. E-mail: rinzler@phys.ufl.edu